Physics-based prognostics of implantable-grade lithium-ion battery for remaining useful life prediction

Yu Hui Lui [a], Meng Li [a], Austin Downey [b,c], Sheng Shen [a], Venkat Pavan Nemani [a], Hui Ye [d], Collette VanElzen [d], Gaurav Jain [d], Shan Hu [a], Simon Laflamme [e,f], Chao Hu [a,f,*]

[a] *Department of Mechanical Engineering, Iowa State University, Ames, IA, 50011, USA*
[b] *Department of Mechanical Engineering, University of South Carolina, Columbia, SC, 29208, USA*
[c] *Department of Civil and Environmental Engineering, University of South Carolina, Columbia, SC, 29208, USA*
[d] *Medtronic Energy and Component Center, Brooklyn Center, MN, 55430, USA*
[e] *Department of Civil, Construction and Environmental Engineering, Iowa State University, Ames, IA, 50011, USA*
[f] *Department of Electrical and Computer Engineering, Iowa State University, Ames, IA, 50011, USA*

HIGHLIGHTS

- We propose a physics-based prognostics approach for battery RUL prediction.
- The approach is applicable to Li-ion batteries used in implantable applications.
- Degradation parameters are estimated from high precision charge curves.
- Destructive analysis is used to validate the degradation parameter estimation.
- Degradation parameters are tracked and forecasted for RUL prediction.

ARTICLE INFO

ABSTRACT

Accurately predicting the remaining useful life (RUL) of a lithium-ion battery is essential for health management of both the battery and its host device. We propose a physics-based prognostics approach for prediction of the capacity and RUL of an implantable-grade lithium-ion battery by simultaneously considering multiple degradation mechanisms, including the losses of active materials of the positive and negative electrodes and the loss of lithium inventory. Unlike traditional capacity-based prognostics that exclusively relies on the empirical capacity fade trend, the proposed approach leverages a half-cell model to 1) estimate degradation parameters from voltage and capacity measurements to quantify the degradation mechanisms and 2) predict the capacity fade trend based on the estimated parameters. We compare the performance of the proposed physics-based approach with that of the traditional capacity-based approach on eight implantable-grade lithium-ion cells that have been subjected to continuous charge–discharge cycling over 1.5 years at high temperature. The proposed approach achieves a more accurate RUL prediction than the traditional capacity-based approach. The results show that the proposed physics-based approach, which extrapolates the degradation parameters, can provide a more accurate and conservative RUL prediction when compared to extrapolating just the capacity.

1. Introduction

Lithium-ion (Li-ion) batteries are widely used not only for their high energy density, high efficiency, and long lifetime but also their production versatility in different sizes and capacities [1–6]. Large-format batteries can be utilized in electric vehicles and grid-connected energy storage systems [2,7,8], whereas small-format batteries can be used in smartphones, tablets, and implantable medical devices [9,10]. Despite their advantages, the performance of Li-ion battery cells decreases over time due to capacity fade and increased internal resistance [1,11]. Typically, a Li-ion battery cell is deemed to reach its end of life when its capacity reduces to 80% of its rated value [1,12]. The remaining useful

life (RUL) of a cell is defined as the available service time before the capacity degrades to a predefined end-of-life limit (or capacity threshold). For a battery-powered device, the battery management system should ideally predict the RUL of each cell before the end of life by using prognostics, which is crucial to ensure reliable operation and minimize the downtime of the device.

Extensive research has been conducted on RUL prediction of general engineered systems over the last decade [13] in relation to data-driven approaches [14–19], model-based approaches [20–24], and hybrid approaches [25–28]. Although these approaches are not specifically intended for application to Li-ion batteries, they can be adapted for the RUL prediction of these batteries. Depending on the cell chemistry and operating conditions, the lifetime of a Li-ion battery cell can range from several months to several years [3,10,29]. As battery degradation is highly dependent on time, future degradation trends can be predicted based on historical data. Therefore, data-driven approaches are attractive provided that abundant historical data are available. As data-driven approaches rely solely on available battery degradation data, prior physical knowledge about battery degradation mechanisms is not necessary [30,31]. Data-driven approaches can capture key degradation information from measurements using black-box models (e.g., machine learning models) to predict the battery RUL [31]. In contrast, model-based approaches use mathematical representations to capture long-term dependencies throughout battery degradation. The models are commonly combined with advanced filtering techniques, such as particle filters, for battery RUL prediction [20,23,24]. Alternatively, hybrid approaches can combine the advantages of data-driven and model-based approaches.

One of the earliest studies on battery prognostics introduced a Bayesian framework with a particle filter for RUL prediction of Li-ion battery cells based on measurements from electrochemical impedance spectroscopy [20]. In this prior work, a relevance vector machine was utilized to learn the evolution of impedance features over time, and the particle filter was used to estimate the RUL with a state-space model based on the measurements. Although the framework shows high prediction accuracy, it requires dedicated equipment for electrochemical impedance spectroscopy. Various subsequent studies have achieved battery prognostics based on voltage and current measurements [21–24]. He et al. [21] used the Dempster–Shafer theory of evidence to initialize the parameters of a capacity fade model using training data and a particle filter to predict the battery RUL. To reduce the uncertainty of this model, Wang et al. [22] simplified its four-coefficient exponential structure into a three-coefficient model by applying a second-order power series approximation to one exponential term in the original formulation. This modified model was based on the observation of the capacity fade trend, achieving robust RUL prediction. Zhang et al. [23] compared a particle filter with three other algorithms, namely, an autoregressive integrated moving average model, a nonlinear degradation autoregressive model, and a regularized particle filter, for RUL prediction based on an exponential model. The particle filter using the exponential model provided higher RUL prediction accuracy than the other algorithms. Likewise, Walker et al. [24] compared a particle filter with a nonlinear least-squares algorithm and an unscented Kalman filter for RUL prediction using a double exponential model. Although an accurate capacity fade model can improve capacity and RUL prediction, these approaches performed poorly when the capacity fade trend switched between multiple models. To address this problem, Hu et al. [10] proposed a hybrid battery prognostics framework that switches between multiple models according to the observed data. This hybrid model consists of two modules: 1) a sparse Bayesian learning module to determine the mapping from charge-related features to capacity measurement and 2) a recursive Bayesian filtering module to both recursively update an empirical capacity fade model using capacity measurements and extrapolate the model for RUL prediction. Switching between multiple models for capacity forecasting provided a higher RUL prediction accuracy compared to single-model RUL prediction.

Most existing battery prognostics approaches simply extrapolate the capacity fade trend for RUL prediction but neglect the underlying degradation mechanisms. Given the complex interactions between degradation mechanisms on the cell capacity, extrapolating the capacity fade trend without considering such mechanisms may notably increase the prediction error [32,33]. Thus, incorporating physical knowledge of the battery degradation mechanisms is important to achieve robust RUL prediction with high accuracy under various degradation scenarios. In a previous study, we investigated a physics-based prognostics approach by using simulated data generated from half-cell curve analysis [33]. We achieved robust RUL prediction by considering the projection over time of three degradation parameters that measure the degree of degradation from representative degradation mechanisms. The parameter projection was performed by applying nonlinear least-squares regression with dynamic bounds. However, the simulated data used to evaluate the half-cell model prevented the validation of the proposed physics-based prognostics approach under real-world settings.

In this paper, we further develop the physics-based prognostics approach by adding a quantitative analysis of the battery degradation mechanisms and experimentally validating the analysis results. We evaluate the effectiveness of the proposed approach for robust RUL prediction on implantable-grade Li-ion battery cells through a 1.5-year cycle aging test in our laboratory. High-quality long-term cycling data are acquired through a high-precision charger that can provide noise-free data [34,35]. The proposed prognostics approach captures degradation trends from three major mechanisms, namely, loss of active material on the positive electrode (LAM$_{PE}$), loss of active material on the negative electrode (LAM$_{NE}$), and loss of lithium inventory (LLI). Specifically, the approach traces the evolution of the corresponding degradation parameters: active masses of the positive electrode (PE) and the negative electrode (NE), m_p and m_n, respectively, and lithium inventory indicator (LII), *LII*. These three degradation parameters are estimated through half-cell curve analysis [36] that examines the voltage–capacity (VQ) curves and the differential voltage (dV/dQ) curves. Given its ability to nondestructively determine the health of a battery cell, half-cell curve analysis has been widely used for Li-ion battery research since its introduction by Bloom et al. [33,34,36–40]. In half-cell curve analysis, a full-cell curve is reconstructed by adjusting the half-cell curves of the PE and NE through the modification of the degradation parameters. Subsequently, the fitting of the reconstructed full-cell curve to the experimental VQ and dV/dQ full-cell curve is achieved by adjusting the half-cell model parameters to obtain a more reliable estimation of the degradation parameters. To validate the estimated degradation parameters obtained from this method, we disassemble the implantable-grade battery cells for building a coin half-cell per electrode (by coupling PEs/NEs with lithium) to calculate the true full-cell active mass.

In a model-based approach, obtaining the degradation trends from the three parameters estimated from experimental data requires the selection of an appropriate method and representation. We adopt the least-squares method given its higher robustness, simplicity, and computational efficiency compared to particle filters [24]. This method can provide accurate representations of the parameters of degradation trends provided that a proper mathematical model is available. After obtaining the coefficients of the mathematical model using training data (from training cells) and applying the least-squares method, we utilize the best-fit model to extrapolate the degradation parameters for capacity and RUL prediction on a test set (containing data from cells other than the training cells).

Using the proposed physics-based prognostics approach, we track the evolution of the three degradation parameters to determine the capacity fade and compare our results to traditional prognostics that only uses capacity fade information. The proposed physics-based prognostics approach enables us to incorporate physical knowledge into the RUL prediction. By doing so, we can clearly identify the root cause of capacity degradation (e.g., which degradation parameter(s) contributed most to

the capacity degradation) especially when the capacity fade trends change course during operation. In addition, we demonstrate the effectiveness of the proposed prognostics approach by bounding the model coefficients during the extrapolation of degradation parameters. The bounded models increase the prediction robustness by regulating the coefficients within predefined ranges in relation to the training dataset and thus prevent overfitting of the relatively complex mathematical models. Moreover, we evaluate the RUL prediction accuracy of the proposed physics-based prognostics approach during the first 30% of the cell lifetime.

The main contributions of this study can be summarized as follows. 1) We develop a quantitative analysis of the degradation mechanisms in implantable-grade Li-ion battery cells considering a 1.5-year cycle aging test at two different discharge rates. 2) The experimental validation of the analysis results is achieved by examining the coin half-cell data of the disassembled aged battery cells. 3) The proposed physics-based prognostics approach improves the accuracy of early prediction of the late-stage fade trend when compared to the capacity-based approach.

The remainder of this paper is organized as follows. Section 2 presents the proposed prognostics approach that comprises the half-cell model, the definition of degradation parameters, the corresponding mathematical models, and the physics-based prognostics applied to capacity and RUL prediction. Section 3 reports the experimental approach to generate battery cell aging data. We report and discuss the results of the proposed approach in Section 4 and draw conclusions in Section 5.

2. Physics-based prognostics approach

2.1. Half-cell model

Various physics-based models have been developed to simulate and analyze the degradation behavior of Li-ion batteries, focusing on the thermal behavior [7,41,42], solid electrolyte interphase (SEI) growth [37,43–45], active material losses [36,38,39,46], and lithium plating [47]. In this study, we used the half-cell model to identify and quantify three commonly reported degradation mechanisms, namely, LAM$_{PE}$, LAM$_{NE}$, and LLI, by reconstructing the measured full-cell VQ curve with positive and negative half-cell curves [36,37,48]. The half-cell model was first introduced by Bloom et al. and later popularized by Dahn's group as a non-destructive approach to diagnosing the degradation of a battery cell. The full-cell VQ curve is denoted as $V_c(Q_c)$, where V_c is the cell voltage and Q_c is the cell capacity. The positive and negative half-cell curves are denoted as $V_p(q_p)$ and $V_n(q_n)$, respectively, and experimentally determined by performing galvanostatic charge–discharge at extremely low C-rates to approach thermodynamic equilibrium (see Section 3.1) with respect to lithium. We approximate the full-cell voltage curve as the difference between the positive and negative half-cell curves:

$$V_c(Q)\big|_{Q=Q_c} \approx V_p(q_p)\big|_{q_p=\frac{Q_c-\delta_p}{m_p}} - V_n(q_n)\big|_{q_n=\frac{Q_c-\delta_n}{m_n}}, \tag{1}$$

where q_p and q_n are the positive and negative specific capacities (mAh/g), respectively, m_p and m_n are the positive and negative active masses (g), respectively, and δ_p and δ_n are the positive and negative half-cell curve slippages (mAh), respectively. Slippage δ_p quantifies the horizontal distance the positive half-cell curve shifts with respect to $Q_c = 0$ mAh, and slippage δ_n quantifies the horizontal distance the left endpoint of the negative half-cell curve shifts with respect to $Q_c = 0$ mAh [33,49]. When δ is positive (negative), the half-cell curve shifts to the right (left) of the origin. The slippages determine the offset $x_{offset} = \delta_p - \delta_n$, between the two half-cell curves, which will later be used to quantify LLI in section 2.2. The active masses in the PE and NE control the capacity (i.e., affect the horizontal span) of the corresponding half-cell curves, which shrink when active mass is reduced. Fig. 1(a) illustrates the effects of slippages on the half-cell model.
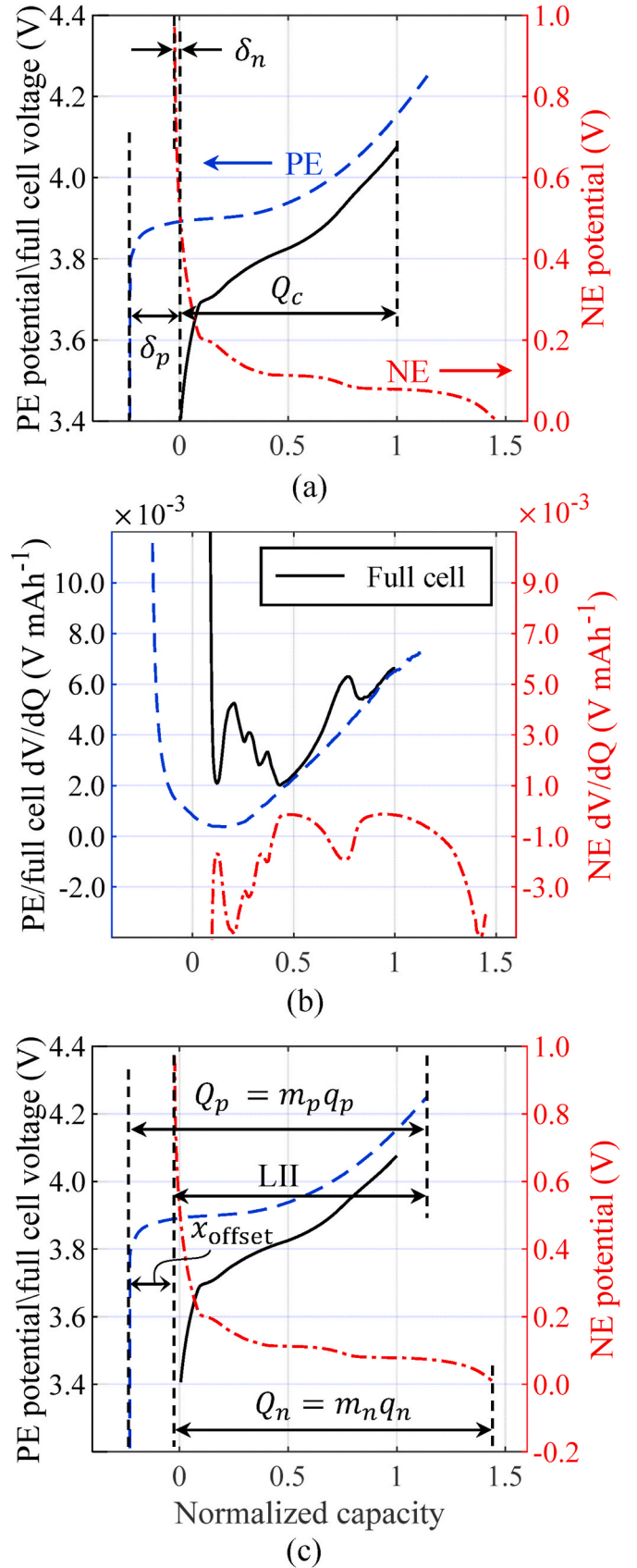

Fig. 1. Examples of (a) half-cell VQ curve analysis, (b) dV/dQ curve analysis, and (c) LII in a half-cell model.

The end of charge (i.e., 100% state of charge) and end of discharge (i. e., 0% state of charge) of a Li-ion battery cell are determined by the maximum and minimum terminal voltages, respectively. In Fig. 1(a), the rising potential of the PE during charge practically limits the end-of-charge voltage of the cell (4.075 V in this study), and the rising potential of the NE during discharge practically limits the end-of-discharge voltage of the cell (3.4 V in this study). The maximum potential in a half-cell curve indicates the limits of the delithiation of that half-cell. We enforce the upper and lower voltage limits (4.075 and 3.4 V, respectively) in the half-cell model and cell aging test (see Section 3.2).

Differentiating Equation (1) to perform dV/dQ analysis [37,48,50] allows for the differential of $V_c(Q)$ to be determined with respect to Q_c over the Q_c curve:

$$\frac{dV(Q)}{dQ}\bigg|_{Q=Q_c} = \frac{1}{m_p}\frac{dV_p(q_p)}{dq_p}\bigg|_{q_p=\frac{Q_c-\delta_p}{m_p}} - \frac{1}{m_n}\frac{dV_n(q_n)}{dq_n}\bigg|_{q_n=\frac{Q_c-\delta_n}{m_n}}. \tag{2}$$

The dV/dQ analysis unveils phase transition information of the electrode materials as identifiable peaks on a charge–discharge VQ curve (Fig. 1(b)) and amplifies small changes in the VQ curve, thus facilitating the identification of the parameters m_p, m_n, δ_p, and δ_n in the half-cell model. However, dV/dQ analysis is susceptible to noise from measurements [39]. Therefore, we use the analysis of the half-cell VQ and dV/dQ curves to robustly characterize and quantify the three degradation mechanisms in a Li-ion battery cell. In Section 4.3, we show that both the VQ and dV/dQ curves are important in the degradation mechanism analysis of implantable-grade Li-ion battery cells.

2.2. Degradation parameters

Various studies have reported the use of the half-cell model to quantify the three degradation mechanisms of Li-ion batteries: LAM_{PE}, LAM_{NE}, and LLI [39,48,50]. The total loss of active mass is the sum of losses of the active mass in the lithiated and delithiated states. However, the loss of lithiated active mass is difficult to quantify because the degree of lithiation of the lost mass is often unknown. Hence, the loss of active mass usually considers the loss in the delithiated state (referred to as LAM in this study), and the loss in the lithiated state usually considers a combination of the loss of delithiated active mass and LLI [39]. Each degradation mechanism can be correspondingly related to a degradation parameter. Moreover, LAM_{PE} and LAM_{NE} can be estimated by tracking the positive and negative active masses, m_p and m_n, respectively.

To estimate the LLI, we define the LII (lithium inventory indicator), which is related to both x_{offset} and m_p:

$$LII = Q_p - x_{offset}, \tag{3}$$

where $Q_p = m_p q_p$ is the capacity of the PE half-cell. Fig. 1(c) illustrates the LII. In a Li-ion battery cell, Li-ions transfer from the NE to the PE during discharge and from the PE to the NE during charge. Physically, the battery cell cannot discharge after the NE has been fully delithiated, because no lithium remains in the NE for transference to the PE. Similarly, the battery cell cannot charge after the PE is "fully delithiated" to the limit of the material structural integrity. Therefore, the LII in Fig. 1 (c) establishes the maximum lithium inventory available in the battery cell containing the left-end of the NE half-cell curve (i.e., NE fully delithiated for discharged cell) and the right-end of the PE half-cell curve (i.e., PE fully delithiated for charged cell). The expression in Equation (3) also indicates that as offset (x_{offset}) becomes increasingly negative (i.e., either PE half-cell curve shifts to the left and/or NE half-cell curve shifts to the right), the rate of LLI increases compared to that of LAM_{PE} in the battery cell. In contrast, as x_{offset} becomes increasingly positive (i.e., either PE half-cell curve shifts to the right and/or NE half-cell curve shifts to the left), the rate of LAM_{PE} increases compared to that of LLI in the battery cell. Practically, the increase of LLI is a result of the accumulation of any parasitic reactions (e.g., the growth of SEI and

delamination of lithiated electrode material) in a battery cell that contribute to lithium inventory loss.

Upon estimation of degradation parameters m_p, m_n, and LII in a battery cell, the appropriate mathematical models should be selected to obtain the parameter trends and subsequently perform physics-based prognostics.

2.3. Empirical degradation models

We use two empirical, simple mathematical models to track the nonlinear trends of both the cell capacity and corresponding degradation parameters. Model I involves two exponential terms and four coefficients:

$$M(t) = \alpha_I \exp(\beta_I t) + \gamma[1 - \exp(\lambda t)], \tag{4}$$

where $M(t)$ is the model output, which can be either the cell capacity or a degradation parameter, t is the time elapsed during the test, α_I, β_I, γ, and λ are model coefficients estimated from measurements. Model I is a variant of the commonly used double exponential model for the capacity-based prognostics of Li-ion batteries [21–24]. Due to its versatility, we obtained high accuracy using this model to fit the LAM_{PE} and LAM_{NE} trends [33]. Model II is a power-law model with two coefficients:

$$M(t) = 1 - \alpha_{II} t^{\beta_{II}}, \tag{5}$$

where α_{II} and β_{II} are the model coefficients estimated from measurements. Model II resembles the common capacity fade model capturing the growth of SEI when $\beta_{II} = 0.5$ (also known as square root of t degradation model) [37,43,46].

2.4. Physics-based capacity and RUL prediction

For physics-based battery prognostics, the coefficients of the empirical degradation models (Section 2.3) should be tuned to accurately track the degradation trends (m_p, m_n, and LII). To this end, we apply the least-squares method to fit the empirical degradation models to the estimated degradation parameters provided that enough measurements are available. However, for prognostics, RUL prediction usually relies on a limited number of measurements from an evaluated (or test) cell. Consequently, the estimated model coefficients might be inaccurate. By considering additional information in a training set of cells that are different from the evaluated cell, the model coefficients can be bounded within predefined ranges [21,24,33]. To investigate the effects of coefficient bounds on capacity and RUL prediction, we consider either the unbounded coefficients from the best-fit model or the coefficients bounded by 50% on the best-fit model. The 50% bounds are selected for consistency with our previous study [33], in which we found the bounds can 1) prevent an empirical degradation model from overfitting the test data especially when predicting in early life and at the same time 2) maintain the adaptability of the model to the test data. Having narrower bounds may reduce the adaptability of the model, while having wider bounds may cause the model to overfit the test data especially in early life when the data is quite limited. These bounding conditions combined with the empirical degradation model I provide two model configurations, which are then implemented in the capacity-based and physics-based approaches (Table 1) to obtain the cell capacity and degradation parameters, respectively. For a third configuration, we consider using 50% bounded coefficients for model II. We omitted the configuration consisting of model II with unbounded coefficients due to its expected poorer performance than model II with bounded coefficients, as observed when comparing configurations 1 and 2. The performance of the three model configurations under the capacity-based and physics-based approaches are evaluated in Section 4.4 in terms of the capacity/degradation parameter and RUL prediction.

We conduct RUL prediction on a test cell (i.e., an evaluated cell

Table 1
Model configurations utilized in this study to predict capacity and degradation parameters.

Modeled parameter	Physics-based approach		
	Configuration 1	Configuration 2	Configuration 3
m_p	Model I, unbounded	Model I, 50% bounded	Model II, 50% bounded
m_n	Model I, unbounded	Model I, 50% bounded	Model II, 50% bounded
LII	Model I, unbounded	Model I, 50% bounded	Model II, 50% bounded
Modeled parameter	Capacity-based approach		
	Configuration 1	Configuration 2	Configuration 3
Capacity	Model I, unbounded	Model I, 50% bounded	Model II, 50% bounded

different from the training cells) with available measurements from the beginning of life (BOL) to test k following the three steps described in Fig. 2. Test k refers to the kth characterization test, where the test data can be used to estimate the degradation parameters of the cell (see Section 3.2 for more details). In the first step, the degradation parameters of the test cell are projected into the future (tests $k + i, i = 1, 2,…$) using one of the model configurations listed in Table 1. The model coefficients are estimated for each of the three degradation parameters using the estimated parameter values up to time k. In the second step, the predicted capacities are simulated by the half-cell model using the predicted degradation parameters. When calculating the capacity of a simulated full-cell curve, it is important to select appropriate voltage cutoffs. We use the lower cutoff voltage of 3.4 V for the battery cells during the cycle aging test (Section 3.2). In addition, we use a lower cutoff voltage of 3.45 V when calculating the simulated capacity from the half-cell model by considering the polarization effect observed at the beginning of charge (voltage curves presented in Section 4.2). In the third step, the earliest time (or test number) at which the predicted capacity becomes less than the end-of-life limit is identified as the end of life, and the RUL is calculated by subtracting the current time (or test number) from the end of life.

Leave-one-out cross-validation is implemented in this study. Predicting the RUL of one cell in an experimental group (e.g., cell C1 in group G4 (see section 3.2 for a description of the experimental setup)) involves three steps. First, we choose one of the model configurations presented in Table 1 and estimate the coefficients of the empirical degradation model for a degradation parameter using its estimates from all other cells in the group (e.g., cells C2–C4 in group G4). These coefficient estimates, together with the coefficient bound setting listed in Table 1, are used to derive the predefined bounds for the degradation model coefficients. Second, the coefficients of the empirical degradation model are estimated by fitting the model to the data from the test cell (e. g., cell G4C1) and the model fitting is constrained by the predefined bounds. Third, the empirical degradation model with its estimated coefficients is used to forecast the future trajectory of the degradation parameter for the test cell. The first three steps are conducted for each of the three degradation parameters. Finally, the forecasted trajectories of the degradation parameters are mapped to a capacity trajectory using the half-cell model and the end-of-life (EOL) of the test cell is estimated as the time when the forecasted capacity trajectory downcrosses an EOL limit. The predicted RUL is the time difference between the current time and the predicted EOL.

The term "physics" in this study refers to tracking the three degradation parameters that allow for a physical interpretation of the major degradation mechanisms driving the degradation of a battery cell. This distinguishes the proposed approach to existing prognostics approaches that simply track the cell capacity. The tracking of the degradation parameters is accomplished by fitting mathematical degradation models, each capturing the evolution of one parameter, to the degradation-parameter estimates via the use of the least-squares method. A set of training data is used only to estimate the coefficients of a best-fit degradation model. These coefficient estimates are then used to define bounds for constraining the model coefficients when fitting the model to test data.
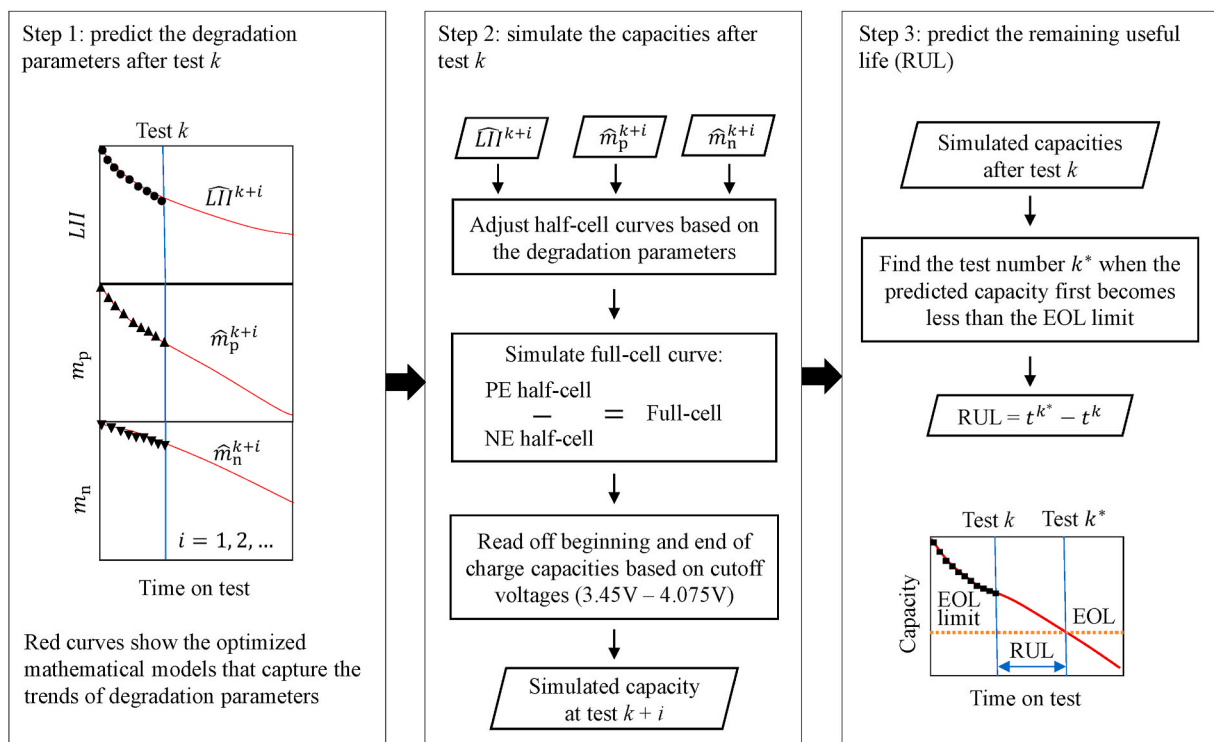

Fig. 2. Flowchart of physics-based capacity and RUL prediction. Here, EOL stands for the end of life.

3. Experimental setup

Implantable-grade Li-ion battery cells obtained from Medtronic are utilized to evaluate the performance of the proposed prognostics approach. A cycling test and characterization test are conducted to age the battery cells and evaluate the capacity and the degradation mechanisms of the cells under different aging conditions, respectively.

3.1. Half-cell curves

The half-cell curves of the PE and NE were obtained from the Medtronic implantable-grade Li-ion battery cells by cycling each electrode separately in a 2325 coin-type cell against lithium at a low C-rate of C/50 and a temperature of 40 °C [37]. The C/50 rate reduces the effect of resistance when estimating the capacity of the battery cell based on the voltage curve. In addition, a low C-rate is required for the half-cell model (Section 2.1). Each coin cell was assembled using a disk electrode punched from an electrode sample, two Celgard 2300 separators, and a lithium foil disk. The electrolyte in the coin cells was 1 M LiPF$_6$ in ethylene carbonate–ethyl methyl carbonate at ratio 3:7 by weight. The positive and negative half-cells were cycled in 3.2–4.25 V and 0.005–1.0 V, respectively.

3.2. Cycling and characterization tests

We conducted the cycle aging test at 55 °C using eight fresh implantable-grade Li-ion battery cells. Applying a relatively high temperature accelerates the capacity fade while maintaining the stability of the battery materials [51]. The eight cells were equally divided into two groups, and each group was tested under a specific discharge condition, as detailed for groups G2 and G4 in Table 2 with discharge rates of C/24 and C/3, respectively. For both groups, we used a constant current of C/3 to charge the battery cells until a cutoff voltage of 4.075 V was reached, at which point the battery cells were charged using a constant voltage of 4.075 V until either the charge current reduced to C/50 or the charge time reached 30 min (illustration of the cycling profile is presented in Fig. 3(c) and (d)). In addition to the cells tested at 55 °C, we conducted another set of cycle aging tests on eight new implantable-grade Li-ion battery cells operating at 37 °C, which is the nominal operating temperature for these cells. Again, we divided these eight cells into two groups, G1 and G3 in Table 2, according to the discharge rates of C/24 and C/3, respectively. Compared to the nominal operating temperature of an implantable-grade cell, 55 °C highly accelerates aging (as further discussed in Section 4.1), and a discharge rate of C/3 highly accelerates capacity fade because the upper usage limit of these battery cells accounts for a nominal discharge rate of C/24 [10].

To use the half-cell model, the VQ curves under slow charge and discharge currents should be obtained. In addition, the characterization test conditions should be equivalent to the half-cell curve test conditions [48]. Hence, we conducted a characterization test on each cell at 40 °C every 2 weeks during approximately the first 3 months and every 4 weeks thereafter. The characterization test included four sequential steps: 1) constant current and constant voltage charge to 4.075 V at C/3 with a cutoff current of C/50, 2) constant current discharge to 3.4 V at C/50 and rest for 30 min, 3) constant current charge to 4.075 V at C/50 and rest for 30 min, and 4) repeated constant current discharge to a voltage corresponding to 10% of the state of charge reduction at C/10

Table 2
Test matrix of cycle aging test.

Group	Charge rate	Discharge rate	Temperature	Number of cells
G1	C/3	C/24	37 °C	4
G2	C/3	C/24	55 °C	4
G3	C/3	C/3	37 °C	4
G4	C/3	C/3	55 °C	4

followed by a 1-h rest period until the cell voltage reached 3.4 V.

We only used the charge data in step 3 of the characterization test for the half-cell curve analysis to determine the degradation parameters in this study. The cycling and characterization tests were conducted using a high precision charger from NOVONIX with a voltage range of 0–5 V and a maximum current output of 2 A for high-quality aging data acquisition [35].

4. Results and discussion

We first present and analyze the capacity fade data measured from the characterization tests. By analyzing the capacity fade and half-cell model, we estimate the three degradation parameters of the battery cells. Subsequently, we validate the estimated parameters based on the aged half-cell voltage curves obtained from the destructive analysis. Finally, we compare the proposed physics-based approach with the capacity-based approach in terms of capacity and RUL prediction accuracies.

4.1. Characterization test results

The charge capacity of the battery cells from the four groups, G1–G4, over time are shown in Fig. 3(a) and (b), where Cx indicates the cell number for $x \in \{1, 2, 3, 4\}$. The charge capacity in Fig. 3 is normalized with respect to that at the BOL to preserve the confidentiality of the true capacity values. The cycling profiles (C-rate vs. normalized capacity) of the C1 cells from the four groups are illustrated in Fig. 3(c) (G1C1 and G3C1) and Fig. 3(d) (G2C1 and G4C1). We present only the cycling profile of the C1 cell in each group as the same cycling profile is used for the other three cells in each group. The 16 cells were continuously cycled for around 1.5 years. We notice an increase in the capacity from the first characterization test to the second characterization test in most battery cells, except for those in group G4. The increase in cell capacity at the initial aging can be attributed to the passive electrode effect, which is observed in battery cells with anode overhang [52]. For the purpose of ensuring the capacities of all the cells have consistently decreasing trends over time, the second characterization test is defined as the BOL. We observe that the cells cycled at low temperature (groups G1 and G3, Fig. 3(a)) have low capacity fade compared with those cycled at high temperature (groups G2 and G4, Fig. 3(b)). Specifically, the cells in groups G1 and G3 maintained 88–94% of their initial capacity, while those in groups G2 and G4 maintained 77–88% of their initial capacity after 1.5 years of charge–discharge from the cycle aging test. The cells cycled at C/24 (groups G1 and G2) exhibit consistently decreasing rates of capacity fade over time (i.e., stable capacity fade throughout aging). In contrast, for the cells cycled with a faster discharge rate (groups G3 and G4), the capacity degradation rates decrease initially but start to increase, which we refer to as capacity fade transition, at around days 200 and 400 for the cells in groups G4 and G3, respectively. This shows that (1) the capacity fade transition is observed at a high C-rate and (2) the occurrence of this transition is delayed at a lower temperature. The exponentially decreasing degradation rates followed by increasing rates during late aging appear to be similar to those reported in various simulation and experimental studies [33,46, 53,54] The underlying degradation mechanism of this transition will be analyzed in section 4.2. All cells within each group exhibit consistent capacity fade trends. As shown in Fig. 3, the cells cycled at the lower C-rate (C/24) share the capacity fade trend with a consistently decreasing rate. In contrast, cells cycled at the higher C-rate (C/3) present two capacity fade trends with an initially decreasing rate of capacity fade followed by an increasing rate, thus posing a challenge for prognostics.

The relation between the capacity degradation rate and temperature can be described by the Arrhenius equation (Equation (S1) in the supplementary material) [55–58], which also allows us to determine the thermal acceleration factor of the implantable-grade Li-ion battery cells
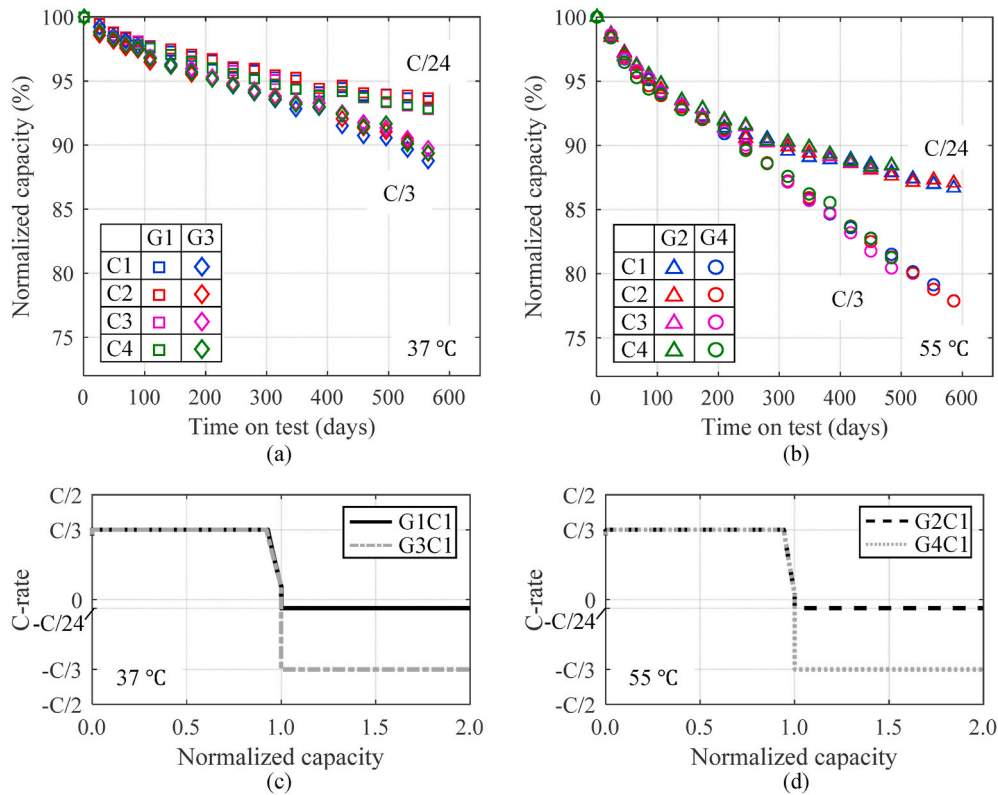
Fig. 3. Capacity fade trends of implantable-grade Li-ion battery cells cycled at (a) 37 °C (groups G1 and G3) and (b) 55 °C (groups G2 and G4) over approximately 1.5 years. The results reflect the data collected during step 3 of the characterization test at the charge rate of C/50. The cycling profiles (C-rate vs. normalized capacity) are illustrated in (c) for cells cycled at 37 °C and (d) for cells cycled at 55 °C. The positive (negative) C-rate indicates the charge (discharge) current.

tested at the two temperatures by using Equation (S2). The cells cycled at C/24 (groups G1 and G2) have a thermal acceleration factor of 1.97, indicating that, on average, the capacity of these cells fades 1.97 times faster at a higher temperature of 55 °C than at a lower temperature of 37 °C. The cells cycled at C/3 (groups G2 and G4) have a thermal acceleration factor of 2.20. Additionally, the activation energies obtained from the Arrhenius equation are 31.903 and 37.108 kJ mol^{-1} for the cells discharged at C/24 and C/3 (See Fig. S1), respectively, are consistent with the values reported in other studies [55,56]. The detailed description of these calculations is presented in the supplementary material. Hereinafter, we disregard the cells cycled at 37 °C from our analysis because their capacity degrades mildly.

4.2. Degradation parameter estimation for cells in groups G2 and G4

To estimate the degradation parameters, the VQ and dV/dQ curves should be carefully analyzed before implementing the half-cell model. The evolution of the experimental VQ and dV/dQ curves for cells C1 in groups G2 and G4 are shown in Fig. 4 as representative examples. The slope of the VQ curve within the lower capacity domain (voltage range of 3.4–3.7 V) of cell C1 in group G2 remains almost unchanged throughout the 1.5-year test (green arrow in Fig. 4(a)), whereas that of cell C1 in group G4 increases as the cell ages (green arrow in Fig. 4(c)). In addition, the flat portion of the voltage curve (i.e., from 3.7 V to 3.8 V) exhibits a significant shift to higher voltage. The increase of the initial voltage and the positive shift of the flat portion of the charge VQ curve for cell C1 in group G4 are likely due to polarization by an increase in the internal cell resistance with aging [3,57,59]. This increase in internal cell resistance can be attributed to electrolyte degradation, SEI growth, and electrode degradation. In addition, the feature locations and magnitudes in the dV/dQ curve of cell C1 in group G2 do not change considerably in the low-capacity domain (green circle in Fig. 4(b)),

whereas they change substantially for cell C1 in group G4 (green circle in Fig. 4(d)). Specifically, the peak increases, and the locations shift to the left as cell C1 in group G4 ages. Finally, the dV/dQ features at the higher normalized capacity of cell C1 in group G4 diminish over time, whereas they remain almost unchanged for cell C1 in group G2. Similar observations can be made for the other cells in both groups.

A deeper analysis of the transitions of the peaks and valleys is required for the half-cell model parameters, m_n, m_p, δ_n, and δ_p, to reflect the VQ and dV/dQ curves. From Ref. [48], we know that the locations of the dV/dQ features are affected by m_n and δ_n, whereas the magnitudes of the dV/dQ features are affected by m_p and δ_p. However, the beginning-of-charge voltage is determined by the negative half-cell curve, while the end-of-charge voltage is determined by the positive half-cell curve (see Fig. 1(a) and Section 2.1). For the cells in group G2, the locations of the dV/dQ features do not change considerably (Fig. 4(b)), but their magnitudes change notably. Therefore, the VQ and dV/dQ curves of the aged cells in group G2 can be reconstructed by varying m_p and δ_p, because m_n and δ_n are not expected to notably change. The locations and magnitudes of the dV/dQ curves for the cells in group G4 (Fig. 4(d)) exhibit considerable changes and should be analyzed more carefully. Considering the peak-to-peak distance, all peaks shift substantially to the left due to the increase in δ_n instead of the decrease of m_n. This is because an increase of the slippage shifts the half-cell curve, whereas a decrease of the active mass shrinks it (see Section 2.2). In addition, the slope of the VQ curves changes at the beginning of charge (Fig. 4(c)), and the first valley disappears in the dV/dQ curve. These characteristics are caused by the reduction of δ_p as a result of LAM$_{PE}$ [39], which shifts the PE half-cell curve to the right, determining the voltage behavior at the beginning of charge [48]. In Fig. 1(b), when the PE half-cell curve shifts to the right (i.e., δ_p decreases), the magnitude of the first valley of the full-cell dV/dQ curve increases. The substantial reduction of δ_p is the result of the LAM$_{PE}$ rate being faster than the LLI
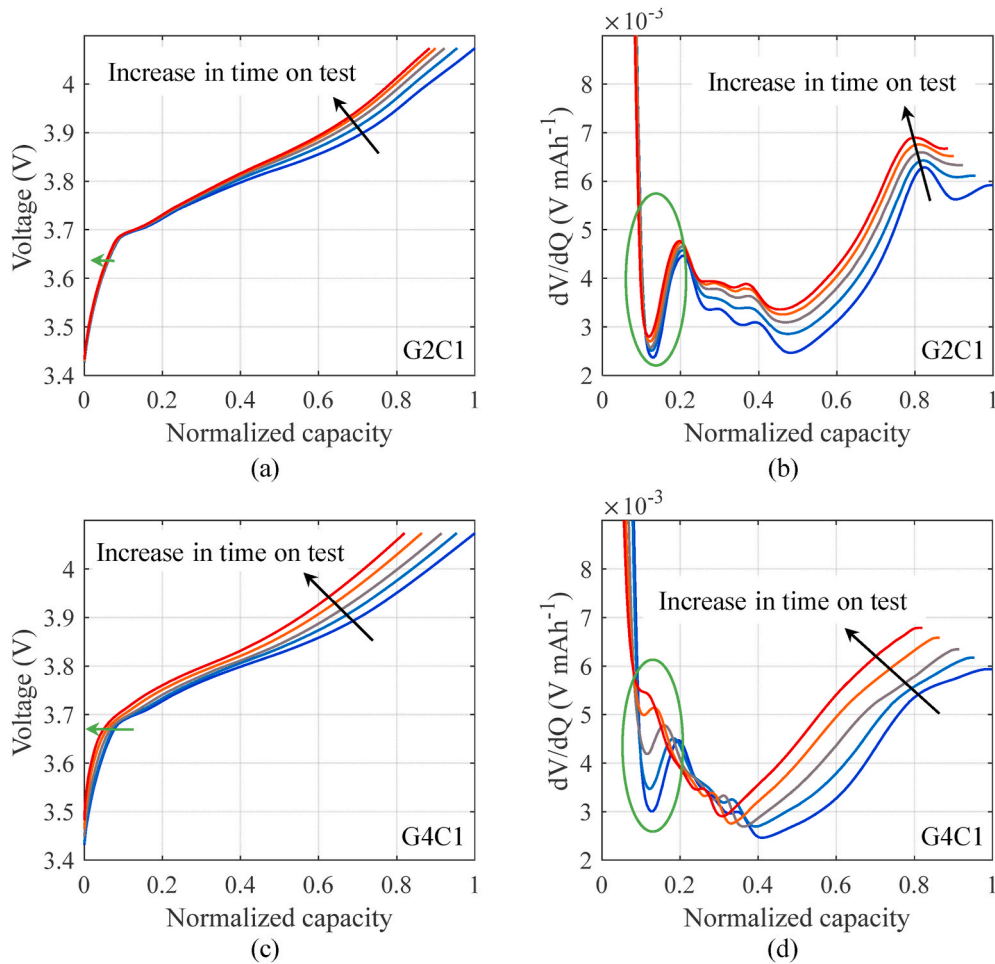
Fig. 4. (a) VQ and (b) dV/dQ curves of cell C1 in group G2. (c) VQ and (d) dV/dQ curves of cell C1 in group G4. The VQ and dV/dQ curves for the other cells in the same group are similar to those shown in this Fig.

rate. These observations provide qualitative guidelines to adjust the half-cell model parameters (m_n, m_p, δ_n, and δ_p) for quantifying the degradation parameters (m_p, m_n, and *LII*).

To determine degradation parameters m_p, m_n, and *LII* at the BOL, we first fit the half-cell model to the VQ curve at the BOL by using the least-squares method. Subsequently, we adjust the four model parameters manually based on the VQ and dV/dQ curves as follows. 1) Adjust m_n and δ_n according to the locations of the dV/dQ features and the voltage of the VQ curve at the beginning of charge. 2) Adjust m_p and δ_p according to the magnitudes of the dV/dQ features and the voltage of the VQ curve at the end of charge. We adopt manual adjustment of the model parameters using the VQ and dV/dQ curves instead of optimization, which can produce the best fitting results based on the VQ curve because the underlying physics interpretation is lost when performing feature evolution through automated parameter optimization (Fig. S2). Although the degradation parameters can be alternatively estimated by applying the least-squares method to the dV/dQ curve using the dV/dQ analysis of the half-cell model, the estimation may be inaccurate due to the disappearance of some of the dV/dQ features as the cells age (green circle in Fig. 4(d)). In fact, lost features may yield a very large error in the degradation parameter estimation if curve fitting is solely based on the similarity of the two curves, namely, the experimental VQ (or dV/dQ) curve and the VQ (or dV/dQ) curve reconstructed from the half-cell model. Moreover, the cutoff cell voltages are not considered when optimizing the degradation parameters using only the dV/dQ curves (Fig. S3). Therefore, we manually adjust the degradation parameters after the BOL considering the potential shortcomings of fitting the VQ

(or dV/dQ) curve using optimization methods.

We analyze the VQ and dV/dQ curves to determine the degradation parameters because the VQ curves allow us to determine the estimation quality through voltage cutoffs, and the dV/dQ curves can improve the adjustment of the degradation parameters in the half-cell model by leveraging obvious features (i.e., peaks and valleys). Even if some dV/dQ features disappear in aged cells, we can manually adjust the parameters by using existing features.

Based on the above qualitative analysis, we used the half-cell model to fit the experimental VQ and dV/dQ curves and quantify the degradation parameters of each cell for every characterization test. Fig. S4 shows the fitted degradation parameters and corresponding capacity per cell in groups G2 and G4. The degradation parameters within each group show a consistent trend. For the cells in group G2 (Figs. S4(a)–(d)), the variation of *LII* is similar to that of the cell capacity, indicating that the main parameter for the capacity fade of these cells is the LLI. In addition, the amount of LAM$_{PE}$ in G2 cells has little effects on the cell capacity given the excessive PE half-cell capacity, indicated as δ_p (positive slippage) in Fig. 1(a). This flat region of the PE half-cell curve acts as a buffer region for LAM$_{PE}$ to affect the cell capacity. Eventually, LAM$_{PE}$ affects cell capacity when δ_p becomes small due to the rate of m_p loss being faster than that of *LII* loss [39]. For the cells in group G4 (Figs. S4(e)–(h)), *LII* follows the cell capacity fade until around day 400 and deviates afterward. This deviation (capacity fade trend transition) is caused by the excessive loss of m_p in comparison to *LII*, which substantially reduces δ_p and, therefore, the end of discharge is determined by positive half-cell curves. As δ_p diminishes to zero, LAM$_{PE}$ can directly degrade the cell

capacity. Based on the half-cell model fitting, all the cells in group G4 exhibit around 32% m_p losses, whereas those in group G2 exhibit approximately 15% losses. In contrast, all the cells in group G4 exhibit around 18% of LII losses, while those in group G2 exhibit about 11% losses.

The half-cell model fitting on days 0 (i.e., BOL) and 484 for groups G2 and G4 are shown in Fig. S5. At the BOL, the fitted VQ and dV/dQ curves suitably agree with the experimental curves. On day 484, the dV/dQ features of the fitted curve remain consistent with the experimental dV/dQ curve, whereas the fitted VQ curves agree with the experimental VQ curves at the beginning and end of charge. This result is important for accurately determining the cell capacity based on the estimated degradation parameters (step 2 of Fig. 2). The deviations of the voltage curve during charge are caused by changes in the PE half-cell curves but not by inaccurate fitting, as explained in Section 4.3. The estimates of degradation parameters through VQ and dV/dQ curve fitting are also validated by comparing the simulated and measured dQ/dV curves (see Fig. S6). We notice that the fitted negative active masses of the fresh G4 cells (i.e., on day 0) are substantially smaller than the values derived based on the negative electrode weights measured by Medtronic. This difference holds even after accounting for the area of negative electrode overhang. We think there may be other internal mechanisms involved in

altering the dV/dQ peak locations that cannot be explained by the half-cell model.

4.3. Destructive analysis

Two aged implantable-grade Li-ion battery cells from each group (G2 and G4) were sent to Medtronic for aged half-cell curve analysis on day 484 to validate the half-cell model fitting. The cells were first discharged to 3.4 V at C/10 and then left alone for several hours before disassembly. The aged cells were disassembled in a dry room to recover the aged PE and NE electrodes. One side of the active material of each electrode was scraped off using N-methyl pyrrolidone to expose the current collector underneath. Subsequently, each electrode with the active material on one side was die-cut into four disk electrodes using a die with a diameter of 12 mm for building a coin cell.

Coin cells of type 2032 were built to evaluate the electrochemical performance of the aged PE and NE half-cells using a construction technique similar to that described in Section 3.1. The four coin cells per aged electrode sample were cycled at C/50 and 40 °C. The cutoff voltages of the positive aged half-cells were 3.0 and 4.2 V, and those of the negative aged half-cells were 0.05 and 1.0 V.

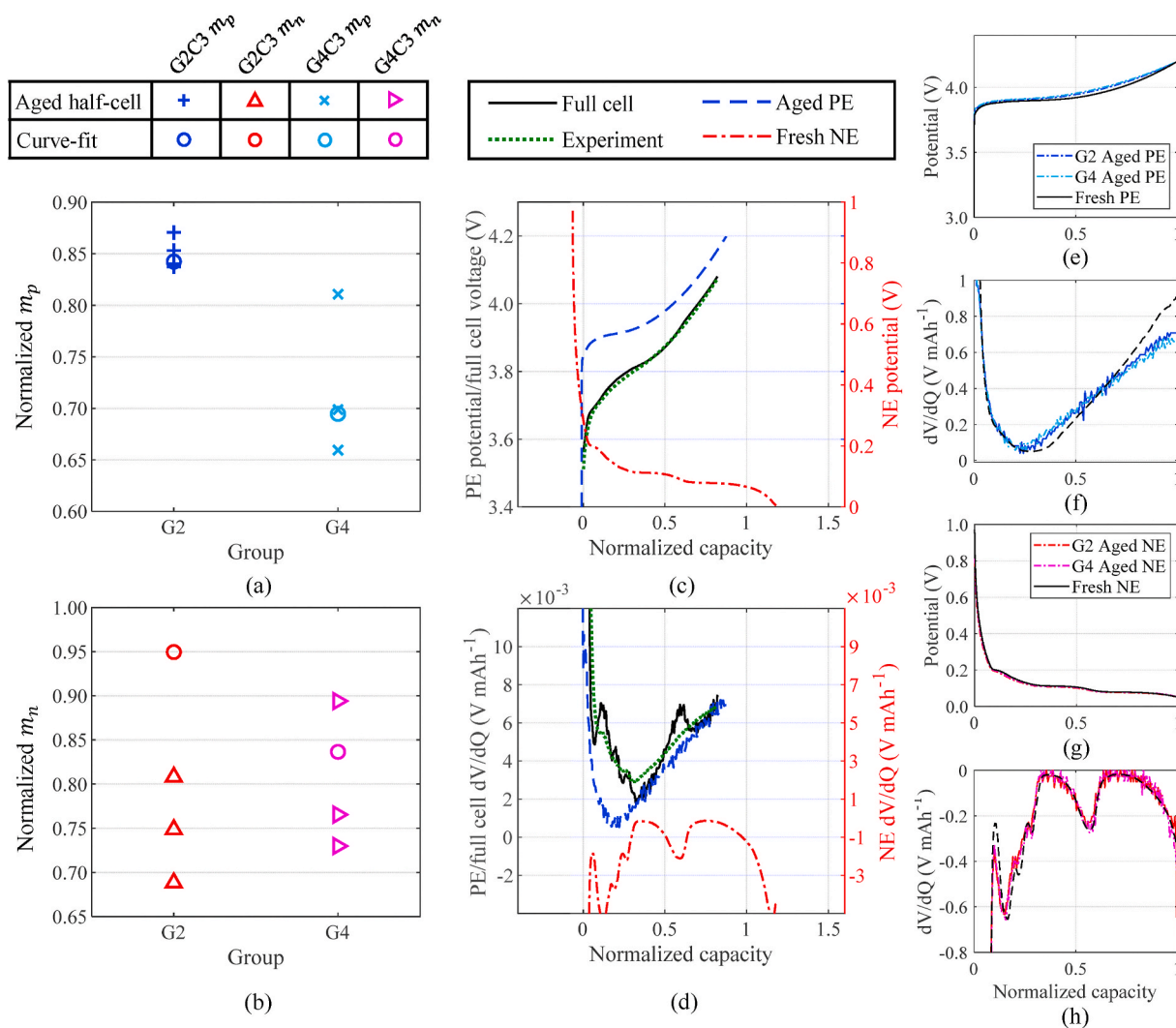The active mass of each electrode in an aged implantable-grade Li-

Fig. 5. (a) PE active mass estimated from the half-cell model (hollow circles) and destructive analysis (crosses) for cells in groups G2 and G4. (b) NE active mass estimated from the half-cell model (hollow circles) and destructive analysis (hollow triangles) for cells in groups G2 and G4. (c) VQ and (d) dV/dQ curves fitted using the half-cell model from aged PE half-cell. (e) VQ and (f) dV/dQ curves of PE fresh half-cell and PE aged half-cells from groups G2 and G4. (g) VQ and (h) dV/dQ curves of NE fresh half-cell and NE aged half-cells from groups G2 and G4.

ion battery cell can be estimated from the aged half-cell curve as follows:

$$m_{\mathrm{AM,\ aged\ half-cell}} = \frac{Q_{\mathrm{aged\ half-cell}}}{q_{\mathrm{fresh}}}, \tag{6}$$

$$A_{\mathrm{ratio}} = \frac{A_{\mathrm{aged\ half-cell}}}{A_{\mathrm{full\ cell}}}, \tag{7}$$

$$m_{\mathrm{AM,\ full\ cell}} = \frac{m_{\mathrm{AM,\ aged\ half-cell}}}{A_{\mathrm{ratio}}}, \tag{8}$$

where $m_{\mathrm{AM,\ aged\ half-cell}}$ (g) is the active mass of the aged half-cell, $Q_{\mathrm{aged\ half-cell}}$ (mAh) is the capacity of the aged half-cell, q_{fresh} (mAh/g) is the specific capacity of the fresh half-cell, $A_{\mathrm{aged\ half-cell}}$ (cm^2) is the coin-cell electrode area of the aged half-cell, $A_{\mathrm{full\ cell}}$ (cm^2) is the electrode area of the full-cell (i.e., implantable-grade Li-ion battery cell), A_{ratio} is the area ratio between $A_{\mathrm{aged\ half-cell}}$ and $A_{\mathrm{full\ cell}}$, and $m_{\mathrm{AM,\ full\ cell}}$ is the estimated full-cell active mass after scaling the coin-cell active mass using A_{ratio}.

Fig. 5(a) shows the PE active mass calculated from the aged half-cell and that estimated from the half-cell model fitted to experimental data. The fitted half-cell model parameter m_{p} (denoted as curve-fit in Fig. 5) mostly agrees with $m_{\mathrm{AM,\ full\ cell}}$ calculated from destructive analysis, suggesting that the degradation parameters obtained from fitting the half-cell model to the experimental VQ and dV/dQ curves closely reflect the true degradation in the cells. Only three out of the four data points are shown for the cells in group G4 because the PE of one of the coin cells was damaged during construction. The corresponding results for the aged NE half-cell are shown in Fig. 5(b). The destructive analysis results do not agree with the curve-fit results because scraping off the electrode materials from the current collector is much more difficult for the NE half-cell than for the PE half-cell. This might have damaged the NE electrode to some extent during the coin cell construction, thus considerably affecting the NE active mass calculated from the aged half-cell curves. The design of the implantable-grade Li-ion battery cell ensures excessive NE active material to prevent both lithium plating when heavy LAM$_{\mathrm{NE}}$ occurs and cell capacity degradation resulting from LAM$_{\mathrm{NE}}$. However, the excessive NE active material may affect the accuracy of the estimated masses using the half-cell model.

To further verify the manual fitting results, we utilized the aged half-cell curve to fit the experimental full-cell curve measured before the cell disassembly. Fig. 5(c), (d) show the fitting results using the aged PE half-cell curves, where the half-cell model better fits the experimental VQ and dV/dQ curves compared with the use of the fresh PE half-cell curves. This is caused by the change in the PE half-cell curve shape (Fig. 5(e), (f)) throughout aging. We use the fresh NE half-cell curves in Fig. 5(c), (d), as the active masses calculated from the aged half-cell do not agree with the curve fitting results. Although the NE dV/dQ feature at the end of the charge region disappears in the full-cell measurement, it can be observed in the aged coin cell. Moreover, data noise can be observed in the aged half-cell curves, which were measured using a lower-precision device instead of the high-precision coulometry used for all the other measurements.

4.4. Capacity and RUL prediction

We obtained the capacity and RUL prediction results using the proposed physics-based prognostics approach and compared them with those using the traditional capacity-based approach. We conducted capacity prediction for the cells in groups G2 and G4, and RUL prediction only for the cells in group G4 because the capacity of the cells in group G2 did not reach a predefined capacity threshold, which we set to 80% of the cell capacity at the BOL.

First, we predicted the degradation parameter trends using the proposed physics-based approach. Provided that the available measurements outnumber the coefficients in the empirical model, the

predictions can be obtained at any inspection point over the lifetime of a battery cell. Fig. S7 illustrates the predicted degradation parameters for cell C1 in group G2 (Fig. S7(a)) and cell C1 in group G4 (Fig. S7(b)) using different model configurations. As all the cells in each group exhibit similar degradation patterns, we selected cell C1 from each group to illustrate and verify the effectiveness of the proposed physics-based approach. Model I with 50% bounds (configuration 2) outperforms its unbounded counterpart (configuration 1) because the high number of model coefficients can cause overfitting of the available measurements from the BOL to the inspection point. Hence, the 50% coefficient bounds prevent overfitting of the least-squares method by limiting the model coefficients to the predefined ranges obtained from the training cells (cells C2–C4 in each group). When predictions were made at day 174, the power-law model with 50% bounds (configuration 3) exhibited better fitting results on all the degradation parameters compared to configurations 1 and 2. This higher accuracy can likely be attributed to the higher model simplicity (only two model coefficients in the power-law model as opposed to four model coefficients in the double exponential model) and the better representation of the trends of the estimated degradation parameters. Properly predicting future degradation parameters is important for accurate cell capacity prediction.

Fig. 6 shows the capacity prediction of cell C1 in group G2 (red square) and cell C1 in group G4 (blue square) on day 174 obtained from the capacity-based approach (Fig. 6(a), (b)) and physics-based approach (Fig. 6(c), (d)). The test data of each cell consists of the past and current measurements of cell capacity that are used to estimate the coefficients of an empirical model. We include the unseen data in the plots mainly for the purpose of visually inspecting the quality of prediction under different configurations. For cells aged at a lower C-rate (group G2), the capacity fade exhibits a consistently decreasing rate, allowing to accurately predict the RUL of the battery cells using the capacity measurements before the end of life. However, at C/24 discharge rate, these implantable-grade battery cells still require several years' aging before the cell capacities degrade to 80% of their initial capacities [60]. Therefore, both evaluated approaches show similar capacity prediction ability for the cells in group G2 (Fig. 6(a) and (c)). Only configuration 3 exhibits relatively accurate capacity predictions for cell G2C1. For cells aged at a higher C-rate (group G4), the capacity fade exhibits an exponential trend with a low fade rate during early aging followed by the rate linearly increasing toward a high value during late aging. As shown in Fig. 7(a), the traditional capacity-based approach cannot predict this transition when a commonly reported square root of t capacity fade model is used. This square root of t model is commonly used to model the capacity fade trend of a Li-ion battery cell as a result of SEI growth [43]. We find that a more general power-law model provides a better representation of the capacity fade trend, consistent with the finding in Refs. [43]. In contrast, the capacity fade of cell G4C1 predicted by the physics-based approach exhibits changes in the trends (Figs. 6(d) and 7(b)), which shows that the proposed physics-based approach allows early prediction of the onset and progression of the late-stage fade rate by tracing the evolutions of the three degradation parameters. By decomposing the cell-level effect (i.e., capacity degradation) into three degradation modes, we incorporated physical knowledge into RUL prediction. As long as the predictions of the three degradation parameters are accurate, we can acquire robust RUL prediction results with the physics-based approach. Fig. 7(b) suggests that the physics-based approach is able to predict the trend transition in the capacity fade during early prediction which is not possible when using the capacity-based approach (Fig. 7(a)). By considering the degradation mechanisms, the physics-based approach can effectively alleviate the risk of early prediction. From Figs. 6(d) and 7(b), we confirm that the physics-based approach can represent a nonlinear capacity fade trend despite the projected degradation parameters being relatively linear. This is attributed to the different effects of the degradation parameters on cell capacity. The physics-based approach can capture such complex degradation effects on the cell capacity through the half-cell model and
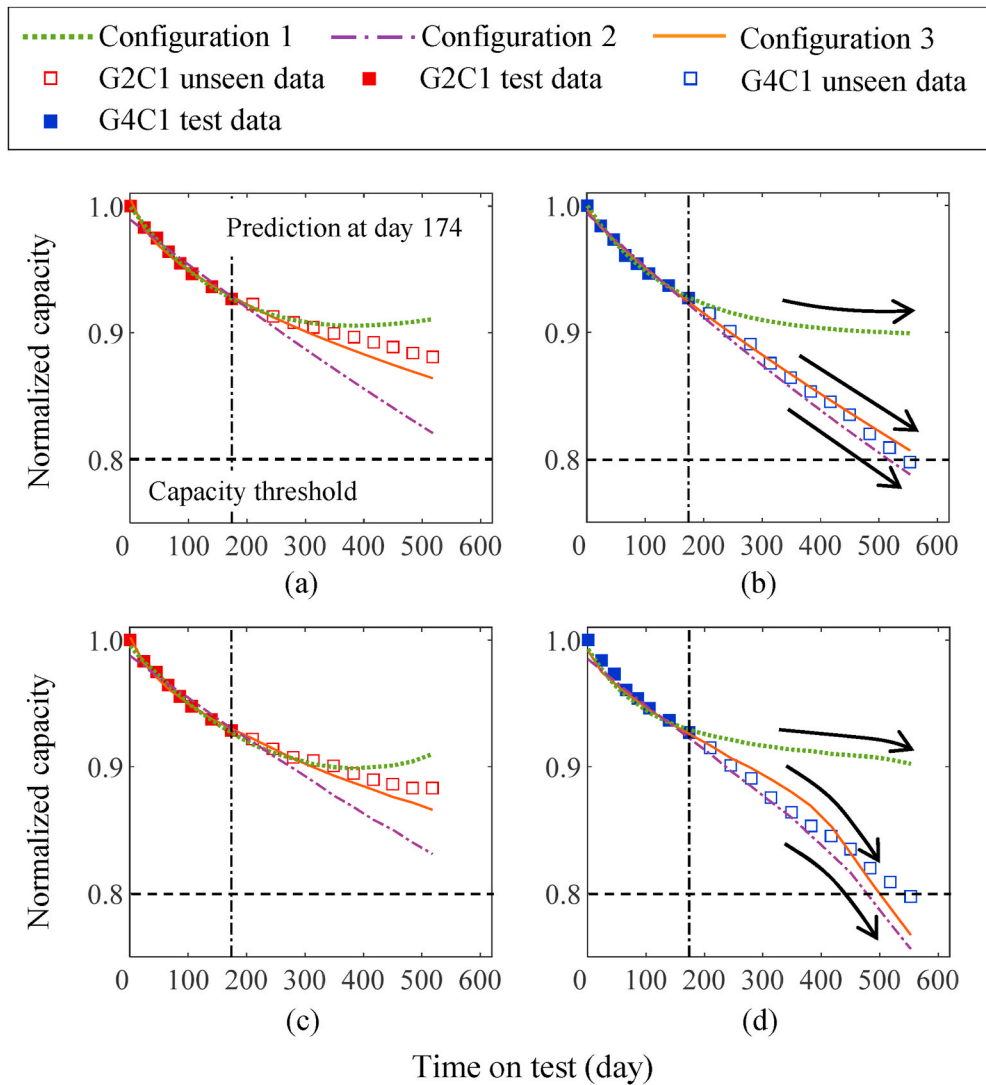
Fig. 6. Capacity prediction obtained from (a), (b) capacity-based approach and (c), (d) physics-based approach for cell C1 in group G2 (red square), and cell C1 in group G4 (blue square). The black arrows in (b) and (d) show the predicted capacity trends by the physics-based approach curve downward due to the consideration of the degradation parameters, whereas the predicted capacity trends by the capacity-based approach solely depend on the available capacity measurements. (For interpretation of the references to colour in this figure legend, the reader is referred to the Web version of this article.)
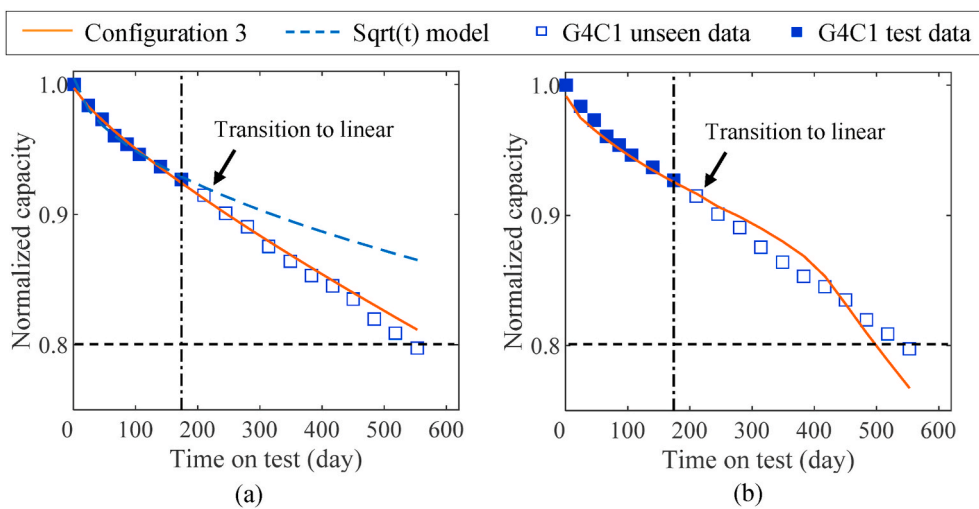

Fig. 7. Capacity prediction using configuration 3 before trend transition of capacity fade (at around day 200) obtained from (a) capacity-based approach and (b) physics-based approach for cell C1 of group G4 on day 174. We also include the commonly used square root of *t* capacity fade model for comparison.
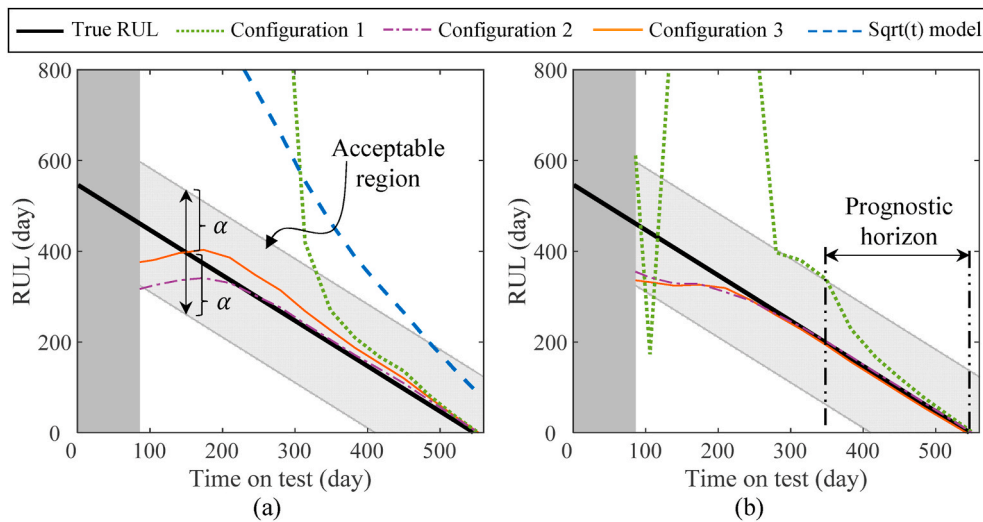
Fig. 8. RUL prediction for cell C1 in group G4 obtained from (a) capacity-based approach and (b) physics-based approach using different model configurations. The grey shaded region around the true RUL line is the acceptable region used to calculate the prognostic horizon.

predict the trend transition in the capacity fade in the early life. Similar to Fig. S7, model I without bounds has the worst performance among the three configurations due to overfitting.

Fig. 8 shows the RUL prediction results for cell C1 in group G4 obtained from the capacity-based (Fig. 8(a)) and physics-based (Fig. 8(b)) approaches. The results are presented as RULs over the cell's lifetime, where 80% of the initial capacity is used as the end of life limit. As model I has four fitting coefficients, the RUL prediction begins on day 86, with at least four measurements being available (prior days are shaded in grey). Generally, the RUL prediction obtained from the physics-based approach converges to the true RUL faster than that obtained from the capacity-based approach. Furthermore, the physics-based approach provides more conservative RUL predictions than the capacity-based approach, that is, for most of the time, the physics-based approach underestimates the RUL of the battery cells. In contrast, the capacity-based approach overestimates the RUL of cell C1 in group G4 for two out of the three configurations. The underestimation of RUL by the physics-based approach is likely due to its ability to predict the transition in the fade trend that is caused by the increasing loss of positive active mass. The overestimation by the capacity-based approach can provide misleading confidence to the user about the cell RUL, which can bring adverse consequences for both the user and manufacturer. In addition, the implementation of coefficient bounds is beneficial as can be seen from the performance differences between configuration 1 and 2.

To quantify how fast the RUL prediction falls within an acceptable region, a metric named prognostic horizon is used [61]. Prognostic horizon is defined as the time difference between when the RUL prediction of a cell first meets a user-defined performance requirement (i.e., an acceptable region) and when the cell reaches its EOL. A graphical illustration of the prognostic horizon is given in Fig. 8(b). In this study, the performance requirement is specified by an allowable error bound (α) around the true RUL, which is calculated by $RUL_{\text{true}}(t) \pm \alpha * EOL$. Fig. 8 illustrates the allowable region when $\alpha = 0.25$. We tested different α values and the results are summarized in Fig. S8. The x-axis represents the width of the allowable region (2*α) and the y-axis represents the prognostic horizon. A longer prognostic horizon suggests the configuration converges faster to the true RUL. From Fig. S8 we can observe that the prognostic horizons of the physics-based approach generally increase faster than those of the capacity-based approach. This means the RULs predicted by the physics-based approach converge faster to the true RULs.

The number of false predictions (false positives and false negatives) given a user-defined acceptable region [61] is also quantified. The

acceptable region for false prediction (see Fig. S9) is defined differently from the one presented in Fig. 8. False positives are unacceptable early predictions and false negatives are unacceptable late predictions. Typically, asymmetric error bounds around the true RUL are used due to the fact that an early prediction of EOL is often preferred over a late prediction of EOL. Fig. S10 shows the number of false positives and false negatives at different acceptable error bounds. Compared to the capacity-based approach, the physics-based approach tends to have larger counts of false positives (unacceptable early predictions) and lower counts of false negatives (unacceptable late predictions). The results suggest that the physics-based approach produces more conservative RUL predictions for the cells in group G4.

The RUL prediction error (in days) listed in Table 3 is defined as the average absolute difference between the predicted and true RUL values:

$$\varepsilon = \frac{1}{K} \sum_{k=1}^{K} \left| Y_k^{\text{true}} - Y_k^{\text{predict}} \right|, \qquad (9)$$

where K is the total number of characterization tests and Y denotes the RUL. The prediction errors in Table 3 correspond to the entire lifetime and first 30% of the lifetime of the cells for the three model configurations obtained using the capacity-based and physics-based approaches. The first 30% of lifetime in this study is defined as the first 30% of the predictable lifetime, where the predictable lifetime is the number of characterization tests starting from the 5th test. The prediction accuracy of the models with coefficient bounds (i.e., configurations 2 and 3) is higher than that of the unbounded models. More importantly, when comparing the prediction errors of the first 30% of the lifetime, the physics-based approach achieved larger prediction accuracy improvement compared with the capacity-based approach, as listed in Table 4. The accuracy improvement (in days) is calculated by subtracting the error of the physics-based RUL prediction from the error of the capacity-based RUL prediction per cell and model configuration: accuracy improvement = $\varepsilon_{\text{capacity-based}} - \varepsilon_{\text{physics-based}}$. Therefore, in Table 4, a positive number indicates an improvement in RUL prediction accuracy, whereas a negative number indicates a reduction in the RUL prediction accuracy for a particular cell and model configuration when using the proposed physics-based approach. Results in Table 4 show that the proposed approach provides higher RUL prediction accuracy than the capacity-based approach for most cells and model configurations.

Table 3

RUL prediction error in days for the entire lifetime and first 30% of the lifetime of each cell in group G4 (C/3 cycling at 55 °C) using capacity-based and physics-based approaches.

Configuration	Prediction error (days) of capacity-based approach							
	Entire lifetime				First 30% of lifetime			
	Cell 1	Cell 2	Cell 3	Cell 4	Cell 1	Cell 2	Cell 3	Cell 4
1	416.27	493.87	436.50	539.71	780.50	791.50	785.50	784.50
2	30.13	41.07	29.00	48.14	89.75	101.25	80.25	102.75
3	33.40	43.13	34.14	59.79	46.00	59.50	29.50	69.50
Configuration	Prediction error (days) of physics-based approach							
	Entire lifetime				First 30% of lifetime			
	Cell 1	Cell 2	Cell 3	Cell 4	Cell 1	Cell 2	Cell 3	Cell 4
1	302.21	132.93	192.86	110.50	510.00	438.00	480.00	286.25
2	20.86	19.73	18.64	30.79	81.00	39.75	45.00	56.25
3	22.36	21.07	26.79	32.71	90.00	21.50	41.50	25.75

Table 4

RUL prediction accuracy improvement in days obtained from the physics-based approach with respect to capacity-based approach for the entire lifetime and first 30% of the lifetime of each cell in group G4.

Configuration	Accuracy improvement (days)							
	Entire lifetime				The first 30% of lifetime			
	Cell 1	Cell 2	Cell 3	Cell 4	Cell 1	Cell 2	Cell 3	Cell 4
1	114.05	360.93	243.64	429.21	270.50	353.50	305.50	498.25
2	9.28	21.33	10.36	17.36	8.75	61.50	35.25	46.50
3	11.04	22.07	7.36	27.07	−44.00	38.00	−12.00	43.75

5. Conclusion

We propose the physics-based prognostics of implantable-grade Li-ion battery cells to track degradation parameters for capacity and RUL predictions. The physics-based approach uses a half-cell model to estimate the degradation parameters from experimental VQ and dV/dQ curves and predict the cell capacity from the estimated parameters. To validate our approach, we use experimental data from 1.5 years of cycle aging tests conducted at two different discharge rates (C/24 and C/3) while setting the temperature to 55 °C for accelerated capacity degradation. In addition, we consider three degradation parameters that correspond to common degradation mechanisms: (1) LAM_{PE}, (2) LAM_{NE}, and (3) LLI. The half-cell curve analysis demonstrates that a faster discharge rate of C/3 induces about 17% more LAM_{PE} in the implantable-grade cells than at a slower discharge rate of C/24, which is validated through destructive analysis. The increased LAM_{PE} for cells discharged at C/3 causes transitions in the fade trends during the 1.5 years of testing, which is not observed for cells cycled at C/24. Specifically, the cells discharged at C/3 show the rate of capacity fade decreases until day 200 and increases thereafter, whereas the cells discharged at C/24 show a consistently decreasing rate of capacity fade over time. After estimating the three degradation parameters using the half-cell model, we use two empirical degradation models, namely a double exponential and a power-law model, to fit the degradation parameters using the least-squares method. The addition of coefficient bounds improves the RUL prediction accuracy during the early life. The main benefit of the proposed physics-based approach is the higher accuracy in the lifetime prediction compared with the traditional capacity-based approach, especially for prediction during the early life. In other words, extrapolating an empirical model using the capacity-based approach can result in high prediction errors during the early life. The physics-based approach, on the other hand, considers the extrapolation of individual parameters associated with various degradation mechanisms, thereby reducing the possibilities of unrealistic predictions during the early life. The physics-based approach could potentially accelerate the screening of new battery materials and the design and development of new battery products. In the future, we plan on investigating prognostics on battery cells tested under actual use conditions. Such conditions may result in different degradation behaviors and capacity fade trends compared with the accelerated test conditions considered in this study.

CRediT authorship contribution statement

Yu Hui Lui: Conceptualization, Methodology, Software, Validation, Investigation. **Meng Li:** Conceptualization, Methodology, Software, Validation, Writing - review & editing. **Austin Downey:** Conceptualization, Software, Writing - review & editing. **Sheng Shen:** Validation, Writing - review & editing. **Venkat Pavan Nemani:** Methodology, Writing - review & editing. **Hui Ye:** Investigation. **Collette VanElzen:** Investigation. **Gaurav Jain:** Conceptualization, Resources, Project administration, Writing - review & editing. **Shan Hu:** Conceptualization, Project administration, Writing - review & editing, Funding acquisition. **Simon Laflamme:** Project administration, Writing - review & editing. **Chao Hu:** Conceptualization, Methodology, Writing - review & editing, Supervision, Project administration, Funding acquisition.

Declaration of competing interest

The authors declare that they have no known competing financial interests or personal relationships that could have appeared to influence the work reported in this paper.

Acknowledgments

Appendix A. Supplementary data

Supplementary data to this article can be found online at https://doi.org/10.1016/j.jpowsour.2020.229327.

References

[1] M.R. Palacín, A. De Guibert, Batteries: why do batteries fail?, American Association for the Advancement of Science, Science 351 (6273) (2016) 1253292, https://doi.org/10.1126/science.1253292, 1253292, Feb. 05.

[2] B. Dunn, H. Kamath, J.M. Tarascon, Electrical energy storage for the grid: a battery of choices, Science (80-.) 334 (6058) (2011) 928–935, https://doi.org/10.1126/science.1212741.

[3] A.J. Smith, H.M. Dahn, J.C. Burns, J.R. Dahn, "Long-Term low-rate cycling of LiCoO2/Graphite Li-ion cells at 55°C, J. Electrochem. Soc. 159 (6) (2012) A705, https://doi.org/10.1149/2.056206jes.

[4] J. O'Heir, Building better batteries, Mech. Eng. 139 (1) (2017) 10–11.

[5] V. Etacheri, R. Marom, R. Elazari, G. Salitra, D. Aurbach, Challenges in the development of advanced Li-ion batteries: a review, Energy Environ. Sci. 4 (9) (2011) 3243, https://doi.org/10.1039/c1ee01598b.

[6] B. Scrosati, J. Hassoun, Y.-K. Sun, Lithium-ion batteries. A look into the future, Energy Environ. Sci. 4 (9) (2011) 3287, https://doi.org/10.1039/c1ee01388b.

[7] K.J. Lee, K. Smith, A. Pesaran, G.H. Kim, Three dimensional thermal-, electrical-, and electrochemical-coupled model for cylindrical wound large format lithium-ion batteries, J. Power Sources 241 (2013) 20–32, https://doi.org/10.1016/j.jpowsour.2013.03.007. Nov.

[8] X. Feng, M. Fang, X. He, M. Ouyang, L. Lu, H. Wang, M. Zhang, Thermal runaway features of large format prismatic lithium ion battery using extended volume accelerating rate calorimetry, J. Power Sources 255 (Jun. 2014) 294–301, https://doi.org/10.1016/j.jpowsour.2014.01.005.

[9] J. Colomer-Farrarons, P. Ll Miribel-Català, A. Ivón Rodríguez-Villarreal, J. Samitier, Portable bio-devices: design of electrochemical instruments from miniaturized to implantable devices, " Accessed: Feb. 24, 2020. [Online]. Available: www.intechopen.com.

[10] C. Hu, H. Ye, G. Jain, C. Schmidt, Remaining useful life assessment of lithium-ion batteries in implantable medical devices, J. Power Sources 375 (Jan. 2018) 118–130, https://doi.org/10.1016/j.jpowsour.2017.11.056.

[11] P. Arora, Capacity fade mechanisms and side reactions in lithium-ion batteries, J. Electrochem. Soc. 145 (10) (1998) 3647, https://doi.org/10.1149/1.1838857.

[12] K.A. Severson, et al., Data-driven prediction of battery cycle life before capacity degradation, Nat. Energy 4 (5) (May 2019) 383–391, https://doi.org/10.1038/s41560-019-0356-8.

[13] C. Hu, B.D. Youn, P. Wang, in: H. Pham (Ed.), Engineering Design under Uncertainty and Health Prognostics, Springer, 2019, pp. 9–10.

[14] J. Liu, A. Saxena, K. Goebel, B. Saha, W. Wang, An adaptive recurrent neural network for remaining useful life prediction of lithium-ion batteries, in: "*Annual Conference of the Prognostics and Health Management Society*, PHM 2010, 2010.

[15] A. Nuhic, T. Terzimehic, T. Soczka-Guth, M. Buchholz, K. Dietmayer, Health diagnosis and remaining useful life prognostics of lithium-ion batteries using data-driven methods, J. Power Sources 239 (2013) 680–688, https://doi.org/10.1016/j.jpowsour.2012.11.146.

[16] J. Wu, C. Zhang, Z. Chen, An online method for lithium-ion battery remaining useful life estimation using importance sampling and neural networks, Appl. Energy 173 (2016) 134–140, https://doi.org/10.1016/j.apenergy.2016.04.057.

[17] M.A. Patil, P. Tagade, K.S. Hariharan, S.M. Kolake, T. Song, T. Yeo, S. Doo, A novel multistage support vector machine based approach for Li ion battery remaining useful life estimation, Appl. Energy 159 (2015) 285–297, https://doi.org/10.1016/j.apenergy.2015.08.119.

[18] Y. Zhang, R. Xiong, H. He, M.G. Pecht, Long short-term memory recurrent neural network for remaining useful life prediction of lithium-ion batteries, IEEE Trans. Veh. Technol. 67 (7) (Jul. 2018) 5695–5705, https://doi.org/10.1109/TVT.2018.2805189.

[19] C. Sbarufatti, M. Corbetta, M. Giglio, F. Cadini, Adaptive prognosis of lithium-ion batteries based on the combination of particle filters and radial basis function neural networks, J. Power Sources 344 (Mar. 2017) 128–140, https://doi.org/10.1016/j.jpowsour.2017.01.105.

[20] B. Saha, K. Goebel, S. Poll, J. Christophersen, Prognostics methods for battery health monitoring using a Bayesian framework, IEEE Trans. Inst. Meas. 58 (2) (2009) 291–296, https://doi.org/10.1109/TIM.2008.2005965.

[21] W. He, N. Williard, M. Osterman, M. Pecht, Prognostics of lithium-ion batteries based on Dempster-Shafer theory and the Bayesian Monte Carlo method, J. Power Sources 196 (23) (Dec. 2011) 10314–10321, https://doi.org/10.1016/j.jpowsour.2011.08.040.

[22] D. Wang, Q. Miao, M. Pecht, Prognostics of lithium-ion batteries based on relevance vectors and a conditional three-parameter capacity degradation model, J. Power Sources 239 (Oct. 2013) 253–264, https://doi.org/10.1016/j.jpowsour.2013.03.129.

[23] L. Zhang, Z. Mu, C. Sun, Remaining useful life prediction for lithium-ion batteries based on exponential model and particle filter, IEEE Access 6 (2018) 17729–17740, https://doi.org/10.1109/ACCESS.2018.2816684. Mar.

[24] E. Walker, S. Rayman, R.E. White, Comparison of a particle filter and other state estimation methods for prognostics of lithium-ion batteries, J. Power Sources 287 (Aug. 2015) 1–12, https://doi.org/10.1016/j.jpowsour.2015.04.020.

[25] J. Liu, W. Wang, F. Ma, Y.B. Yang, C.S. Yang, A data-model-fusion prognostic framework for dynamic system state forecasting, Eng. Appl. Artif. Intell. 25 (4) (2012) 814–823, https://doi.org/10.1016/j.engappai.2012.02.015. Jun.

[26] L. Liao, F. Köttig, A hybrid framework combining data-driven and model-based methods for system remaining useful life prediction, Appl. Soft Comput. J. 44 (Jul. 2016) 191–199, https://doi.org/10.1016/j.asoc.2016.03.013.

[27] Y. Song, D. Liu, C. Yang, Y. Peng, Data-driven hybrid remaining useful life estimation approach for spacecraft lithium-ion battery, Microelectron. Reliab. 75 (Aug. 2017) 142–153, https://doi.org/10.1016/j.microrel.2017.06.045.

[28] Y.Z. Zhang, R. Xiong, H.W. He, M. Pecht, Validation and verification of a hybrid method for remaining useful life prediction of lithium-ion batteries, J. Clean. Prod. 212 (2019) 240–249, https://doi.org/10.1016/j.jclepro.2018.12.041. Mar.

[29] R.R. Richardson, M.A. Osborne, D.A. Howey, Gaussian process regression for forecasting battery state of health, J. Power Sources 357 (2017) 209–219, https://doi.org/10.1016/j.jpowsour.2017.05.004.

[30] L. Wu, X. Fu, Y. Guan, Review of the remaining useful life prognostics of vehicle lithium-ion batteries using data-driven methodologies, Appl. Sci. 6 (6) (May 2016) 166, https://doi.org/10.3390/app6060166.

[31] Y. Li, et al., Data-driven health estimation and lifetime prediction of lithium-ion batteries: a review, in: Renewable and Sustainable Energy Reviews, vol. 113, Elsevier Ltd, 2019, p. 109254, https://doi.org/10.1016/j.rser.2019.109254. Oct. 01.

[32] J.C. Burns, et al., Predicting and extending the lifetime of Li-ion batteries, J. Electrochem. Soc. 160 (9) (2013) A1451–A1456, https://doi.org/10.1149/2.060309jes.

[33] A. Downey, Y.-H. Lui, C. Hu, S. Laflamme, S. Hu, Physics-based prognostics of lithium-ion battery using non-linear least squares with dynamic bounds, Reliab. Eng. Syst. Saf. 182 (2019), https://doi.org/10.1016/j.ress.2018.09.018.

[34] A.J. Smith, J.R. Dahn, Delta differential capacity analysis, J. Electrochem. Soc. 159 (3) (2012) A290, https://doi.org/10.1149/2.076203jes.

[35] Cyclers. http://www.novonix.ca/cyclers, 2020. (Accessed 6 April 2020).

[36] I. Bloom, A.N. Jansen, D.P. Abraham, J. Knuth, S.A. Jones, V.S. Battaglia, G. L. Henriksen, Differential voltage analyses of high-power, lithium-ion cells 1. Technique and application, J. Power Sources 139 (1–2) (2005) 295–303, https://doi.org/10.1016/j.jpowsour.2004.07.021.

[37] R. Fathi, J.C. Burns, D.A. Stevens, H. Ye, C. Hu, G. Jain, E. Scott, C. Schmidt, J. R. Dahn, Ultra high-precision studies of degradation mechanisms in aged LiCoO2/Graphite Li-ion cells, J. Electrochem. Soc. 161 (10) (2014) A1572–A1579, https://doi.org/10.1149/2.0321410jes.

[38] K. Ando, T. Matsuda, D. Imamura, Degradation diagnosis of lithium-ion batteries with a LiNi0.5Co0.2Mn0.3O2 and LiMn2O4 blended cathode using dV/dQ curve analysis, J. Power Sources 390 (April) (2018) 278–285, https://doi.org/10.1016/j.jpowsour.2018.04.043.

[39] C.R. Birkl, M.R. Roberts, E. McTurk, P.G. Bruce, D.A. Howey, Degradation diagnostics for lithium ion cells, J. Power Sources 341 (2017) 373–386, https://doi.org/10.1016/j.jpowsour.2016.12.011.

[40] Y.H. Lui, M. Li, M. Sadoughi, C. Hu, S. Hu, Physics-Based State of Health Estimation of Lithium-Ion Battery Using Sequential Experimental Design, 2018, https://doi.org/10.1115/detc2018-86358. Aug.

[41] U. Selokar, Q. Qiao, H. Lu, PCM and the thermal model in battery design, in: IEEE Int. Conf. Electro Inf. Technol., 2019, pp. 596–600, https://doi.org/10.1109/EIT.2019.8833702, 2019-May,.

[42] K. Kumaresan, G. Sikha, R.E. White, Thermal model for a Li-ion cell, J. Electrochem. Soc. 155 (2) (2008) A164, https://doi.org/10.1149/1.2817888.

[43] P.M. Attia, W.C. Chueh, S.J. Harris, Revisiting the t 0.5 dependence of SEI growth, J. Electrochem. Soc. 167 (9) (May 2020) 90535, https://doi.org/10.1149/1945-7111/ab8ce4.

[44] B. Khanal, B. Bahrami, H. Lu, Q. Qiao, Modelling of Solid Electrolyte Interface (SEI) layer of lithium-ion batteries using kinetic Monte Carlo approach, in: 67th Annual Conference and Expo of the Institute of Industrial Engineers 2017, 2017, pp. 1193–1198. Accessed: Nov. 02, 2020. [Online]. Available: https://search.proquest.com/docview/1951122245?fromopenview=true&pq-origsite=gscholar.

[45] H. Ekstrom, G. Lindbergh, A model for predicting capacity fade due to SEI formation in a commercial graphite/LiFePO4 Cell, J. Electrochem. Soc. 162 (6) (2015) A1003–A1007, https://doi.org/10.1149/2.0641506jes.

[46] Q. Zhang, R.E. White, Capacity fade analysis of a lithium ion cell, J. Power Sources 179 (2) (2008) 793–798, https://doi.org/10.1016/j.jpowsour.2008.01.028.

[47] X.G. Yang, Y. Leng, G. Zhang, S. Ge, C.Y. Wang, Modeling of lithium plating induced aging of lithium-ion batteries: transition from linear to nonlinear aging, J. Power Sources 360 (2017) 28–40, https://doi.org/10.1016/j.jpowsour.2017.05.110.

[48] H.M. Dahn, a.J. Smith, J.C. Burns, D.a. Stevens, J.R. Dahn, User-friendly differential voltage analysis freeware for the analysis of degradation mechanisms in Li-ion batteries, J. Electrochem. Soc. 159 (9) (2012) A1405–A1409, https://doi.org/10.1149/2.013209jes.

[49] K. Honkura, K. Honbo, Y. Koishikawa, T. Horiba, State analysis of lithium-ion batteries using discharge curves, ECS Trans. 13 (19) (2008) 61–73, https://doi.org/10.1149/1.3018750.

[50] C. Hu, H. Hong, Y. Li, H.L. Jeong, On-board analysis of degradation mechanisms of lithium-ion battery using differential voltage analysis, in: Proceedings of the ASME Design Engineering Technical Conference, 2A, Dec. 2016, https://doi.org/10.1115/DETC2016-59389, 2016.

[51] L. Lu, X. Han, J. Li, J. Hua, M. Ouyang, A review on the key issues for lithium-ion battery management in electric vehicles, J. Power Sources 226 (2013) 272–288, https://doi.org/10.1016/j.jpowsour.2012.10.060.

[52] M. Lewerenz, J. Münnix, J. Schmalstieg, S. Käbitz, M. Knips, D.U. Sauer, Systematic aging of commercial LiFePO4|Graphite cylindrical cells including a theory explaining rise of capacity during aging, J. Power Sources 345 (Mar. 2017) 254–263, https://doi.org/10.1016/j.jpowsour.2017.01.133.

[53] R. Spotnitz, Simulation of capacity fade in lithium-ion batteries, J. Power Sources 113 (1) (Jan. 2003) 72–80, https://doi.org/10.1016/S0378-7753(02)00490-1.

[54] X. Lin, J. Park, L. Liu, Y. Lee, A.M. Sastry, W. Lu, A comprehensive capacity fade model and analysis for Li-Ion batteries, J. Electrochem. Soc. 160 (10) (2013) A1701–A1710, https://doi.org/10.1149/2.040310jes.

[55] T. Waldmann, M. Wilka, M. Kasper, M. Fleischhammer, M. Wohlfahrt-Mehrens, Temperature dependent ageing mechanisms in Lithium-ion batteries - a Post-Mortem study, J. Power Sources 262 (2014) 129–135, https://doi.org/10.1016/j.jpowsour.2014.03.112.

[56] B.Y. Liaw, E.P. Roth, R.G. Jungst, G. Nagasubramanian, H.L. Case, D.H. Doughty, Correlation of Arrhenius behaviors in power and capacity fades with cell impedance and heat generation in cylindrical lithium-ion cells, J. Power Sources 119 (121) (2003) 874–886, https://doi.org/10.1016/S0378-7753(03)00196-4.

[57] M. Uno, K. Tanaka, Accelerated charge-discharge cycling test and cycle life prediction model for supercapacitors in alternative battery applications, IEEE Trans. Ind. Electron. 59 (12) (2012) 4704–4712, https://doi.org/10.1109/TIE.2011.2182018.

[58] A.M. Bizeray, S. Zhao, S.R. Duncan, D.A. Howey, Lithium-ion battery thermal-electrochemical model-based state estimation using orthogonal collocation and a modified extended Kalman filter, J. Power Sources 296 (2015) 400–412, https://doi.org/10.1016/j.jpowsour.2015.07.019.

[59] P. Keil, S.F. Schuster, J. Wilhelm, J. Travi, A. Hauser, R. Karl, A. Jossen, Calendar aging of lithium-ion batteries, J. Electrochem. Soc. 163 (9) (2016) A1872–A1880, https://doi.org/10.1149/2.0411609jes.

[60] S. Shen, M. Sadoughi, X. Chen, M. Hong, C. Hu, A deep learning method for online capacity estimation of lithium-ion batteries, March, J. Energy Storage 25 (2019) 100817, https://doi.org/10.1016/j.est.2019.100817.

[61] A. Saxena, J. Celaya, E. Balaban, K. Goebel, B. Saha, S. Saha, M. Schwabacher, Metrics for evaluating performance of prognostic techniques, in: 2008 Int. Conf. Progn. Heal. Manag., IEEE, 2008, pp. 1–17.